Batch Production of High-Quality Graphene Grids for Cryo-EM: Cryo-EM Structure of *Methylococcus capsulatus* Soluble Methane Monooxygenase Hydroxylase

Eungjin Ahn[1]†, Byungchul Kim[1]†, Soyoung Park[1,6], Amanda L. Erwin[2,3], Suk Hyun Sung[4], Robert Hovden[4,5], Shyamal Mosalaganti[2,3], Uhn-Soo Cho[1]*

[1]Department of Biological Chemistry, University of Michigan, Ann Arbor, Michigan 48109, USA

[2]Department of Cell and Developmental Biology, University of Michigan, Ann Arbor, Michigan 48109, USA

[3]Life Sciences Institute, University of Michigan, Ann Arbor, Michigan 48109, USA

[4]Department of Materials Science and Engineering, University of Michigan, Ann Arbor, Michigan 48105, USA

[5]Applied Physics Program, University of Michigan, Ann Arbor, Michigan 48105, USA

[6]Department of Fine Chemistry, Seoul National University of Science and Technology, Seoul 139-743, Korea

Abstract

Cryogenic electron microscopy (cryo-EM) has become a widely used tool for determining protein structure. Despite recent technology advances, sample preparation remains a major bottleneck for several reasons, including protein denaturation at the air/water interface, the presence of preferred orientations, nonuniform ice layers, etc. Graphene, a two-dimensional allotrope of carbon consisting of a single atomic layer, has recently gained attention as a near-ideal support film for cryo-EM that can overcome these challenges because of its superior properties, including mechanical strength and electrical conductivity. Here, we introduce a reliable, easily implemented, and reproducible method to produce 36 graphene-coated grids within 1.5 days. To demonstrate their practical application, we determined the cryo-EM structure of *Methylococcus capsulatus* soluble methane monooxygenase hydroxylase (sMMOH) at resolutions of 2.9 and 2.4 Å using Quantifoil and graphene-coated grids, respectively. We found that the graphene-coated grid has several advantages, including less amount of protein required and avoiding protein denaturation at the air/water interface. By comparing the cryo-EM structure of sMMOH with its crystal structure, we identified subtle yet significant geometrical changes at the non-heme di-iron center, which may better indicate the active site configuration of sMMOH in the resting/oxidized state.

Introduction

Single-particle cryogenic electron microscopy (cryo-EM) has evolved as a major technique to determine high-resolution protein structure. Advances in multidisciplinary technologies including direct electron detectors, energy filter systems, advanced algorithms, and data collection/processing strategies have enabled cryo-EM to become a versatile and routine method for the structure determination of biomacromolecules (Bai et al., 2015; Dubochet, 2012; Kühlbrandt, 2014; Lawson et al., 2020; Scheres, 2012; Zivanov et al., 2018).

With these advances and the broad adoption of cryo-EM techniques in instrument development and software algorithms, specimen preparation and grid development have become increasingly important for determining protein structures by cryo-EM (Gardiner et al., 2021; Naydenova et al., 2020; Rice et al., 2018). Several challenges remain in cryo-EM sample preparation, such as protein denaturation mediated by the air/water interface (AWI), nonuniform ice thickness, preferred particle distributions/orientations, and beam-induced motion (Arsiccio et al., 2020; D'Imprima et al., 2019; Drulyte et al., 2018; Glaeser, 2016; Sun, 2018; Tan et al., 2017). To overcome these challenges, the addition of a continuous thin layer of supporting film on the cryo-EM grid has been widely considered and tested; film materials include inorganic metal alloys (e.g., titanium–silicon and nickel–titanium), carbon nanomembranes, and other forms of amorphous carbon (Huang et al., 2020; Llaguno et al., 2014; Rhinow et al., 2011; Rhinow and Kühlbrandt, 2008; Russo and Passmore, 2016). However, these films typically add significant background noise to the microscopic images. Other types of supporting films, such as a lipid monolayer and two-dimensional (2D) streptavidin crystals, have been successfully employed to determine protein structures (Han et al., 2012; Kelly et al., 2010, 2008; Ma et al., 2016; Yu et al., 2016); however, technical challenges have limited their availability and applicability.

An ideal supporting film for cryo-EM grids must have several properties. First, the material must be thin and sufficiently transparent that it does not interrupt the electron beam pathway to minimize

unwanted scattering. Second, it should be physically strong enough to stably hold both a thin ice layer and particles during screening and data collection. Finally, it should be electrically conductive to prevent charge accumulation on the surface during lengthy automated data collection. Graphene, a 2D single atomic carbon layer, meets most of the conditions for use as a supporting film, as it possesses electrical conductivity (~15,000 $cm^2 \cdot V^{-1} \cdot s^{-1}$), optical transparency (~97.7%), mechanical strength (~1,000 GPa), and minimal scattering events under a 300 kV electron beam (Bai et al., 2010; Grigorenko et al., 2012; Lee et al., 2008; G.-H. Lee et al., 2013; Novoselov et al., 2004). A plasma-treated graphene grid has been shown to achieve more evenly distributed particles in ice and minimize beam-induced particle motion (Russo and Passmore, 2014).

Several research groups recently attempted to coat EM grids with graphene or its derivatives to exploit those superior properties for cryo-EM observation (Benjamin et al., 2016; D'Imprima et al., 2019; Fan et al., 2019; Han et al., 2020; Liu et al., 2019; Naydenova et al., 2019; Palovcak et al., 2018; Wang et al., 2020; Yao et al., 2020). Although these earlier attempts were successful, the methods they used are not easily adopted at the laboratory level for several reasons. 1) Some of the reported methods require professional instruments, such as chemical vapor deposition (CVD) equipment for graphene synthesis and a Langmuir–Blodgett trough for uniform graphene oxide coating (Cote et al., 2009; Wang et al., 2020). In addition, it is necessary to collaborate with an expert in graphene or its derivatives during its synthesis, transfer, and modification. 2) Only a few established methods are available for assessing the quality of graphene-coated grids (Kumar et al., 2021; Liu et al., 2019; Naydenova et al., 2019).

Here, we report a versatile and easy fabrication method for developing graphene-coated grids. We focused on developing a robust graphene-coating protocol for grids that is reproducible and easy to follow. Using a new method, we routinely prepared 36 graphene-coated grids at once in ~1.5 days. We also focused on establishing proper validation methods to evaluate the success of the graphene-coating process on the grid.

To test the applicability and quality of the graphene-coated grids, we determined the cryo-EM structures of *Methylococcus capsulatus* (*M. caps*) soluble methane monooxygenase hydroxylase (sMMOH) using the newly developed graphene-coated grid. Methanotrophic bacteria in ambient environments use methane as their sole carbon source by converting methane to methanol. The critical enzymes participating in this conversion are two types of methane monooxygenases; particulate methane monooxygenase (pMMO) and soluble methane monooxygenase (sMMO). In particular, sMMO participates in the following reaction:

$$CH_4 + O_2 + 2H^+ + 2e^- \rightarrow CH_3OH + H_2O$$

The effectiveness of catalysis by sMMO depends on the interplay of four protein components: sMMO hydroxylase (sMMOH), sMMO reductase (sMMOR), sMMO regulatory subunit (sMMOB), and sMMO inhibitory subunit (sMMOD). The crystal structure of sMMOH, exhibits a 251 kDa heterohexameric ($\alpha_2\beta_2\gamma_2$) architecture with a glutamate- and histidine-coordinated di-iron active site in each α protomer (Rosenzweig et al., 1993). sMMOR shuttles electrons from reduced nicotinamide adenine dinucleotide (NADH) to the di-iron center of sMMOH (Kopp et al., 2001). sMMOB is an auxiliary component that modulates the reduction potentials at the di-iron center and facilitates substrate availability at the active site (Lee et al., 2013; Paulsen et al., 1994). Another regulatory component, sMMOD, inhibits the catalytic activity of sMMOH (Kim et al., 2019; Merkx and Lippard, 2002). To date, all 28 structures of sMMOH deposited since 1993 have been determined solely by X-ray crystallography (Banerjee et al., 2019; Rosenzweig et al., 1993; Sazinsky and Lippard, 2006; Sirajuddin and Rosenzweig, 2015). However, X-ray structures can be affected by high precipitant concentrations and crystal packing. To obtain the atomic-resolution structure without unnatural compounds and crystal contacts, we determined the cryo-EM structure of *M. caps* sMMOH at resolutions of 2.9 and 2.4 Å using Au Quantifoil and the newly developed graphene-coated grid, respectively.

Results and Discussion

Making graphene-coated Au Quantifoil grids. The graphene transfer approach we developed and adopted is based on the polymer-film-assisted transfer method instead of the polymer-free transfer method (Lin et al., 2019; Suk et al., 2011; Zhang et al., 2017). Although the polymer-free transfer method has several advantages (for example, it can produce a hyperclean graphene surface and graphene with high-order crystallinity), skills and knowledge are required for interfacial control between the transfer solvents, and thus the method is not suitable for those who are unfamiliar with the handling of graphene and surface engineering. By contrast, polymer-assisted graphene transfer has several advantages that make it possible to overcome these challenges. 1) It provides an intuitive and easy-to-use method of generating graphene-coated Au Quantifoil grids (i.e., graphene grids) at the laboratory level for those who are unfamiliar with nanomaterials. 2) It can be used for the mass production of high-quality graphene grids with good surface coverage (>95%) and cleanness. It takes 1.5 days to generate a batch of 36 graphene grids using the method we developed. The method requires a petri dish, an oven, a 25 mm × 25 mm PMMA/graphene pad (ACS Material), acetone, and a 3D-printed graphene transfer tool that we designed and developed (Figure S1). The graphene grid synthesis process is described in detail in the Experimental Details section (Movie S1) and illustrated in Figure 1. We note that the baking step (200 °C, overnight) in the oven was crucial for producing graphene grids with clean surfaces (Figure S2). The boiling point of the PMMA rinsing solvent (i.e., acetone) is 56 °C. However, we found that a moderate baking temperature (100 °C) was not sufficient to remove the swelled solvent in the PMMA residues (Figure S2a). We recommend performing the baking step without vacuum assistance, as oxygen species facilitate the removal of PMMA residues during this process (Figure S2b). By increasing the temperature to 200 °C, we minimized the residual PMMA on the graphene surface without damaging the coated graphene (Figure S2c) (Park et al., 2012; Pirkle et al., 2011). The extension of baking time to 48 hr barely improved cleanness (Figure S2d). Although residual PMMA on the graphene surface is

inevitable because it adheres to surface defects/boundaries during graphene synthesis by CVD (Pathak et al., 2017), it can be minimized by the high-temperature baking process (Zhang et al., 2020). We also noticed that two layers of protection (the lid of the glass petri dish and the beaker) during overnight baking prevent direct exposure to heat and thus minimize the damage to the graphene and the holey carbon. Both copper and gold Quantifoil grids were examined to test which grid material is more suitable for the graphene coating procedure (Figure S3). We found that the Au Quantifoil grid exhibits better graphene coating because the Cu Quantifoil grid become heavily oxidized during baking, as indicated by color change and more damage to the graphene/Quantifoil holey carbon during overnight baking at 200 °C.

Characterization of the graphene grid. Previous studies in generating graphene-/graphene-oxide-coated grids have demonstrated the coating quality by testing and visualizing standard macromolecules such as the 30S ribosomal subunit and apo-ferritin using cryo-EM (Benjamin et al., 2016; Han et al., 2020; Naydenova et al., 2019). Although this approach may indirectly indicate the quality of graphene or graphene-oxide grids, some or all of the cryo-EM data must be used to examine the quality of the grids, which is time-consuming and poses a potential risk to the precious specimen on the grid. Therefore, easily applied quality control/validation tools are urgently needed before sample application. As quality control tools for the graphene grids, we employed four approaches: SEM, bright-field (BF) TEM, Raman spectroscopy, and AFM.

The graphene-coated Au Quantifoil grids were characterized using SEM and BF TEM to examine the coverage and surface quality. First, we compared the untreated PMMA/graphene-coated Au Quantifoil grids (before PMMA removal) and PMMA-free graphene grids. As shown in Figure 2d, the surface of the PMMA/graphene grid was fully covered with a thick PMMA layer (approximately 500 nm according to the product information), which even blocked the observation of the hole patterns in the commercial Quantifoil grid (Au 300 mesh, R1.2/1.3). The TEM image

and selected area electron diffraction (SAED) pattern of the PMMA/graphene grid (Figure 2e,f) showed a strong scattering pattern of amorphous carbon, which originated from the covered PMMA layer, and the characteristic SAED pattern of monolayer graphene (Figure 2f) (Elango et al., 2011; Zhang et al., 2014). After PMMA removal by rinsing and baking, most of the thick PMMA layer was eliminated from the graphene surface, as confirmed by SEM, BF TEM, and SAED observations (Figure 2g–i). The SEM image indicates that the graphene fully covers the hole-patterned carbon of the Au Quantifoil grid. The SAED diffraction image further demonstrates that the diffraction pattern of the amorphous carbon ring is minimized, except for residual signals originating from the supporting holey carbon film of the Quantifoil grid. The graphene transfer method seems to be applicable to various other types of EM grids, but the Au Quantifoil showed the best graphene coverage (>95%) and cleanness. We note that materials with larger mesh number and smaller hole diameter showed better graphene coverage and less damage to the graphene grids during baking. Smaller hole diameters have also been shown to minimize beam-induced particle motion (Naydenova et al., 2020). The annular dark-field scanning TEM (ADF-STEM) mode and SAED patterns were further examined to visualize the clearness and validate the single-layered graphene on Au Quantifoil grid. ADF-STEM on a single hole region of graphene-coated grid confirmed that there was minimal amount of amorphous residues present (Figure S4). These residues were not detectable in SAED patterns (Figure S5). The SAED pattern were achieved in the position- and size-controlled aperture (800 nm) of the graphene-coated gird enough to show the suspended graphene region without any amorphous carbon background. In PMMA/graphene-coated grid, the SAED pattern displayed the bright background signal coming from the amorphous carbon of the thick PMMA layer. After rinsing 3 times in acetone and a backing step, only graphene peak signals were detected (Figure S5e, f), which further supports the cleanness of the graphene surface after treatment. The single-tilt SAED accumulation method was adopted to demonstrate the single-layered graphene-coated grid (Figure S6). The 3D electron diffraction probed reciprocal out-of-

plane (k_z) structure of Bragg rods and confirmed that the specimen is a monolayer with distinctive out-of-plane features.

Figure S7 shows the Raman spectra of commercial monolayer graphene on Cu foil (Graphenea; top), the commercial Quantifoil grid (Electron Microscopy Sciences; middle), and the in-house built graphene-coated grid (bottom). Single-layer graphene without defects was confirmed in the commercial monolayer graphene Cu grid by observing the absence of the D peak (1348 cm^{-1}; defect-induced second-order Raman scattering) as well as the high peak intensity ratio between the G peak (1580 cm^{-1}; in-plane vibrations of sp^2-hybridized carbon atoms) and the 2D peak (2670 cm^{-1}; second-order overtone of a different in-plane vibration) (Ferrari and Basko, 2013; Tan et al., 2012). It is generally acknowledged that a Raman intensity ratio of the 2D and G peaks (I_{2D}/I_G) of >2.0 denotes single-layer graphene (Lin et al., 2015; Wu et al., 2014). The Raman spectra of the commercial Quantifoil grid (before graphene transfer) shows large, broad D and G bands, which are derived from the hole-patterned amorphous carbon (Malard et al., 2009). After graphene transfer to the Quantifoil grid, the I_{2D}/I_G was 7.2, which coincides with other characterizations of single-layered graphene (Table S1). Raman spectra of the graphene layer and the D and G band patterns of the Quantifoil grid appear in the graphene-coated grid indicates that the graphene monolayer was successfully transferred and coated on the Quantifoil grid.

AFM was further employed to characterize the morphology and physical properties of the graphene grids. The Quantifoil grid has regularly patterned holes, which were fully covered after the PMMA/graphene transfer process (Figure S8). After the thick PMMA layer was removed, the hole pattern covered by graphene appeared, with minimal surface residues (Figure S8e,f); most of the areas of interest (cryo-sample positions) were clean and defect-free. The graphene grids exhibited a relatively large *z*-scale variation (300 nm), mainly because of a fragile grid wrinkle that occurred during AFM sample preparation. Inside of the graphene-covered holes, the surface was flat and clean, and showed low *z*-scale variation (10 nm) (Figure S8g,h). Therefore, the Raman spectroscopy

and AFM results, in addition to SEM and TEM images, can be good validation tools for examining the quality of graphene-coated grids after graphene transfer and before specimen application.

Cryo-EM structure determination of *M. caps* sMMOH. Since Rosenzweig and coworkers determined the first crystal structure of *M. caps* sMMOH in 1993, the structures of different enzymatic stages of sMMOH have been determined by X-ray crystallography (Merkx et al., 2001; Rosenzweig et al., 1993; Whittington et al., 2001; Whittington and Lippard, 2001). Earlier studies indicated that the geometry of the non-heme di-iron center plays a critical role in indicating the enzymatic stage of sMMOH. The di-iron geometry, which is coordinated by two histidines (His147 and His246) and four glutamates (Glu114, Glu144, Glu209, and Glu243), undergoes subtle yet significant conformational changes depending on its catalytic reaction stage and its association with auxiliary subunits (e.g., MMOB and MMOD) (Kim et al., 2019; Lee et al., 2013). This rearrangement of the di-iron coordination is interlocked and triggered by the movement of the four-helix bundle (helices B, C, E, and F) that contain these two histidines and four glutamates. Although currently available crystal structures of sMMOH have provided valuable information regarding di-iron coordination shifts under various circumstances, protein crystallization requires high precipitant concentrations and unnatural compounds, and the protein structure can be further constrained by crystal contacts. To illustrate the structure of sMMOH in solution and validate the general applicability of the graphene-coated grid, we determined the cryo-EM structures of *M. caps* sMMOH at resolutions of 2.9 and 2.4 Å using the Au Quantifoil and graphene-coated grids, respectively, under normal buffer conditions [30 mM HEPES (4-(2-hydroxyethyl)-1-piperazineëthanesulfonic acid), pH 7.0, 150 mM NaCl, and 1 mM TCEP (tris(2-carboxylethyl)phosphine)] (Figures 3a–c and S9).

Structural comparison of sMMOH determined using Au Quantifoil and graphene-coated

grids. Purified sMMOH at concentrations of 1.3 and 0.5 mg/mL was applied to the Au Quantifoil and graphene-coated grids, respectively (Table S2). A total of 3075 (Au Quantifoil grid) and 3880 (graphene grid) raw movie stacks were collected using 300 kV Titan Krios with a K3 direct electron detector equipped with a BioQuantum energy filter (Figures 3a and S9a). Particles of 2.1 M (Au Quantifoil grid) and 4.2 M (graphene grid) were obtained after particle selection using the TOPAZ program (Bepler et al., 2020). After iterative 2D and 3D classification using cryoSPARC (Figures 3b and S9b) (Punjani et al., 2017), 479k and 325k particles were selected for the Au Quantifoil grid and graphene grid to reconstitute the cryo-EM structures of sMMOH at resolutions of 2.9 and 2.4 Å, respectively, after real-space refinement by PHENIX (Table S3, Figures 3c and S9c) (Afonine et al., 2012). The 2.4 Å cryo-EM structure of sMMOH obtained using the graphene grid shows clear side chain densities throughout the entire structure, including the non-heme di-iron center (Figure 3e). The Rosenthal–Henderson plot indicates that the quality and behavior of the final selected particles from the graphene grid are slightly better than those of the particles from the Au Quantifoil grid (Figure 3d). Although about 7.7% of total particles (325K out of 4.2M) were used in the graphene grid dataset for the final refinement compared to 22.8% in the Au Quantifoil dataset (479K out of 2.1M), 843K particles before the hetero-refinement of the graphene grid dataset (20%) also showed the B factor of 97.0, which is higher than 325K particles yet still lower than that of the Au Quantifoil dataset. We also noted that the graphene grid requires approximately five times less protein to obtain a similar number of particles (Table S2). Although we found that sMMOH exhibited a preferred orientation on the graphene grid, this orientation might be caused in part by the molecular nature of sMMOH, which has a flat shape (Figures 3b,c and S10). It is not clear why the specimen on the graphene grid exhibits better behavior than that on the Au Quantifoil grid, but one possible explanation might be the minimal particle exposure to the AWI. Because particles adhere to the graphene surface after plasma treatment, exposure to the AWI can be dramatically reduced. Russo and Passmore also demonstrated that a plasma-treated graphene grid reduces the

beam-induced particle motion, which may further contribute to resolution improvement (Russo and Passmore, 2014). However, the final refined structures of sMMOH on the Au Quantifoil and graphene grids are almost identical, suggesting that structural perturbation by the graphene layer is negligible (Figure S9d). The Cα root-mean-square (rms) difference in the two structures is 0.338 Å, and they have nearly identical di-iron center geometries (Figures 3f,g and S9d).

Particle distribution of sMMOH on the graphene-coated grid using c ryo-electron tomography. Bio-macromolecular particles tend to adhere to the oxidized hydrocarbon surface after the plasma treatment of graphene or amorphous carbon layers. This allows the particles to populate and stick on the grid surface during cryo-EM and negative-stain EM sample preparation. Since particles are not exposed to the air-water interface after attachment to the oxidized graphene layer, this further provides an additional advantage in data quality by preventing protein denaturation induced by the air-water interface. To visualize particle distribution on the graphene-coated grid, we analyzed cryo-electron tomograph data of plunge-frozen sMMOH particles on graphene-coated and Au Quantifoil grids. As shown in Figure 4, sMMOH particles are densely populated on the convex-shaped graphene surface. The same protein concentration of sMMOH (0.24 mg/ml) was applied to prepare the Au Quantifoil grid, but most of particles were attracted to the amorphous carbon and barely detectable within the grid hole (Figure S11, Movies S2, S3). This observation agrees well with the previous cryo-electron tomography result of 1-pyrene carboxylic acid on chemically oxidized graphene-coated grids using (D'Imprima et al., 2019). Therefore, the cryo-electron tomography data of the graphene-coated grid further supports that the graphene-coated grid not only concentrates particles on the surface but also prevents the protein denaturation mediated by the air-water interface.

Structural comparison of sMMOH determined by cryo-EM and X-rays. To evaluate potential structural perturbation during crystallization, we compared the X-ray and cryo-EM structures of

sMMOH. We adopted the X-ray structure of sMMOH in the oxidized/resting state (PDB ID: 1MTY) for comparison (Rosenzweig et al., 1997). Purified sMMOH was crystallized under buffer conditions of 25 mM Li_2SO_4, 50 mM NH_4OAc, and 5% polyethylene glycol (PEG 4000), and its structure was determined at a resolution of 1.7 Å. The structural overlay of the crystal structure (PDB ID: 1MTY) and cryo-EM structure (graphene grid) of sMMOH exhibit a Cα rms difference of 0.351 Å, indicating that the overall architecture of the two structures is very similar (Figure S12). However, we observed differences in the di-iron position and surrounding di-iron coordinating residues (Figure 5). First, we observed differences in the positions of both irons. Fe_1^{3+} and Fe_2^{3+} were shifted by 0.5 Å (protomer1)/0.2 Å (protomer2) and 1.1 Å/0.6 Å, respectively, in the cryo-EM structure compared to the X-ray structure (Figure 5). The distance between the two γ carboxyl groups of Glu114 and Glu243 also changed, from 5.5 Å/4.4 Å (protomer1) and 5.6 Å/4.6 Å (protomer2) in the X-ray structure to 5.5 Å/5.5 Å (protomer1) and 5.9 Å/5.4 Å (protomer2) in the cryo-EM structure. This result indicates that two γ carboxyl groups of Glu114 and Glu243 moved away from each other in the cryo-EM structure, which resulted in the changes in the positions of the two irons, particularly that of Fe_2. The iron–iron distances also increased from 3.0 Å (protomer1) and 3.1 Å (protomer2) to 3.2 and 3.2 Å, respectively. The difference we observed here can be derived from the crystal packing since the geometry of the di-iron center is greatly influenced by the four-helix bundle (Figure 3f; helices B, C, E, and F), whose conformation might be restricted by the crystal packing in the X-ray structure. We further observed an unidentified cryo-EM density on top of the di-iron center, where the substrates had been located (Figure S13) (Kim et al., 2019; Sazinsky and Lippard, 2005; Whittington et al., 2001). A similar density was also observed in several crystal structures of sMMOH, but one of the crystallization compounds was assigned to refine the structure (e.g., acetate, in PDB ID: 1MMO) (Rosenzweig et al., 1993). This result indicates that this increase in density might be attributable to one of the sMMOH substrates or molecules involved in the catalytic reaction of sMMOH, which might be co-purified during protein

purification. Regardless of the type of compound, it certainly participates in di-iron coordination in the resting state of sMMOH (Figure S13). Because we were not able to identify the nature of this compound, we decided not to build a model of this density.

Conclusions

In this paper, a versatile method of developing graphene-coated EM grids (i.e., graphene grids) was established using various in situ characterization tools to assess the quality. This method does not require professional skills or expensive instruments and is easily applied to commercially available EM grids with minimal polymeric residues and high coverage. Moreover, high-quality graphene coatings were obtained after cleaning and baking steps. The graphene grids were tested by determining the cryo-EM structure of *M. caps* sMMOH at a resolution of 2.4 Å. We conclude that the graphene grid has advantages for cryo-EM structure determination because it requires five times less protein and avoids protein denaturation mediated by the AWI.

Materials and Methods

Protocol for graphene transfer to cryo-EM grid. A 25 mm × 25 mm poly(methyl methacrylate) (PMMA)/graphene pad (Trivial Transfer Graphene™, SKU# TTG10011) was purchased from ACS Material and stored in a 2–8 °C refrigerator before use. The graphene transfer process was based on the user instructions with several modifications. First, 36 gold Quantifoil holey carbon grids (Au R1.2/1.3 Quantifoil grids)(the amorphous carbon layer facing up) were placed on a three-dimensional (3D)-printed grid transfer tool (Figure S1) immersed in deionized water in a petri dish, and the PMMA/graphene/support textile pad was gently placed on the water surface to prevent water overflow onto the graphene layer. Direct water overflow onto the graphene layer will cause it to shrink, making it unusable. The supporting textile was gently pushed to the bottom of the petri dish using tweezers. This procedure separated the graphene layer from the textile pad and caused

the graphene layer to float on the water surface (Figure 1, Movie S1). Then the PMMA/graphene layer was carefully matched with the top of the 36 grids using tweezers, and the structure was slowly removed from the water by lifting the grid transfer tool. Residual water in the grid transfer tool was drained with a cleaning wipe, and the PMMA/graphene/grid structure was placed in an oven (100 °C, 30 min) to dry completely. This step also increased the contact between the graphene layer and grids. Fully dried PMMA/graphene-coated grids were individually detached from the grid transfer tool and immersed in acetone solvent (50 °C, 30 min, repeated three times with mild stirring) in a petri dish to dissolve and eliminate the PMMA layer (do not use any plastic/polymer materials to touch the acetone solution). The acetone-free, air-dried, PMMA-free graphene grids were transferred to a microscope slide glass and baked in the oven (200 °C, 24 h) to evaporate the remaining solvent and swell the polymers on the graphene. To prevent the direct exposure of the graphene grids to heat, we placed the slide glass in a petri dish (glass, with a lid) and also covered it with a glass beaker during baking. The generated graphene grids were individually transferred to a grid box, which was held in a desiccator for up to several months before use. All procedures described here is also available in Movie S1 and the following link (http://www.uscho-lab.com/research/).

Characterizations of graphene grids. Scanning EM (SEM) images were obtained using a NOVA NanoLab 200 instrument with an electron beam power of 5 kV at 0.40 nA. The graphene and other grids were placed on a grid-holding accessory for SEM observation. Transmission EM (TEM) images were obtained at 200 kV using a JEOL-2010F instrument. Raman spectra were collected using a Renishaw instrument equipped with a 532 nm diode laser having a power of 0.5 W; a 1200 lines/mm grating and an Olympus SLMPlan 20× objective lens was also used. All spectra were obtained in the Raman shift range of 1000–3000 cm^{-1} to analyze the framework bands and at peak positions of 2680 cm^{-1} to analyze the 2D band and 1580 and 1380 cm^{-1} to monitor the G and D

peaks of graphene (amorphous carbon bands), respectively. The laser was calibrated in static scan mode using a silicon standard.

Electron microscopy for SAED and tilting measurement. TEM and SAED were performed on Thermo Fisher Talos operated at 200 kV equipped with Gatan OneView camera. For 3D electron diffraction, 31 SAED patterns were collected across –15° - +15° range then mapped to 3D reciprocal space to reveal graphene was monolayer. ADF-STEM was performed at 200 kV with 10.5 mrad convergence semi angle.

Atomic force microscopy (AFM). AFM images were taken using a Veeco Dimension Icon atomic force microscope with a ScanAsyst-Air AFM tip from Bruker Nano Inc. The sample grids were held on a slide glass by copper tape/slide glass during scanning with vacuum-assisted lock on slide glass. The data were analyzed using Nanoscope Analysis 2.0 software. The AFM tip was calibrated in thermal tune mode with a spring constant of 0.4 N/m.

Purification of *M. caps* sMMOH. *M. caps* (Bath) sMMOH was purified as described in the literature (Lee et al., 2013). In brief, *M. caps* (Bath) was cultured in a nitrate mineral salt medium at 30 °C. Then the harvested cells were collected by centrifugation (11,300*g*) for 20 min at 4 °C. The cell pellet suspended in the buffer was lysed at 4 °C (CV334, Sonics), and the lysate was centrifuged at 30,000*g* for 45 min at 4 °C. The supernatant was collected and filtered through a 0.22 μm membrane. The filtrate was loaded onto DEAE Sepharose, Superdex 200, and finally Q Sepharose columns to obtain sMMOH with >95% purity.

Cryo-EM sample preparation on graphene grids. Before sample loading, the graphene grids were treated by glow discharge (PELCO easiGlow, Ted Pella Inc.) at 5 mA for 60 s in vacuum (<0.26 mbar). Cryo-EM sample grids were prepared in a Vitrobot Mark IV instrument (Thermo Fisher Scientific), which was set to 4 °C at 100% humidity. Purified protein solution (3 μL) was loaded onto the graphene surface of the graphene grid or holey carbon surface of the Au Quantifoil

grids as indicated. After 30 s, the grids were blotted for 4 s with a blot force of 0 and immediately plunged into precooled liquid ethane for vitrification.

Data acquisition. A total of 3880 (graphene grid) and 3075 (Au Quantifoil grid) raw movie stacks were automatically collected on a 300 kV Titan Krios using a K3 direct electron detector (with a BioQuantum energy filter, Gatan) at the Pacific Northwest Center for Cryo-EM (PNCC). Raw movies from Quantifoil and graphene grid were collected in K3 super-resolution mode at a magnification of 81,000× (slit width 20 eV, spot size 5, C2 aperture 50 μm) with a super-resolution pixel size of 1,027 and 1.059 Å, respectively. The total exposure time was 3.4 s at 0.85 $e^{-}/Å^2$ per frame to generate 60-frame gain-normalized microbial reverse-electrodialysis cell stacks. The total dose per stack were 49 and 51 $e^{-}/Å^2$ for Quantifoil and graphene grid, respectively[2].

Cryo-EM data processing and model refinement. All processing was completed in RELION and cryoSPARC (Punjani et al., 2017; Scheres, 2012). The MotionCor2 implemented in RELION corrected the initial drift and beam-induced motion, and Gctf was used to measure the contrast transfer function (CTF) (Zhang, 2016). Following CTF estimation, micrographs were manually inspected, and those with outliers in the defocus value, ice thickness, or astigmatism, as well as micrographs with lower predicted CTF-correlated resolution (>5 Å), were removed from further processing. The initial set of particles was selected using Topaz (Bepler et al., 2020). The selected particles were further 2D- and 3D-classified by iterative classification and selection rounds in cryoSPARC using an *ab initio* 3D reconstructed model as a starting reference. A total of 325k and 479k particles were chosen to build final 3D reconstruction maps with a resolution of 2.31 and 2.60 Å ($FSC_{0.143}$) for the graphene grid and Au Quantifoil grid, respectively (Figure S14). Using the crystal structure of sMMOH (PDB ID: 1MTY), we refined the structures using real-space refinement in the PHENIX program and COOT (Afonine et al., 2012; Emsley and Cowtan, 2004; Rosenzweig et al., 1997). The reported resolutions of the final maps (2.4 Å for the graphene grid and 2.9 Å for the Au Quantifoil grid) were estimated using the map versus model FSC curves

($FSC_{0.5}^{map\ vs.\ model}$) in phenix.xtriage (Afonine et al., 2012). UCSF Chimera was used to visualize the EM density and obtain illustrations for figures (Pettersen et al., 2004).

Cryo-electron tomography. The same concentration of sMMOH (0.24mg/ml) was used to make both Au Quantifoil and graphene-coated grids. Vitrified specimens were imaged with a 300 kV Titan Krios G4i transmission electron microscope equipped with a K3 summit direct electron detector and a Gatan energy filter. The magnification was set to a pixel size of 2.122Å for tilt series collected from the Au Quantifoil and graphene-coated grids. Dose-fractionated images were automatically recorded using SerialEM (Mastronarde, 2005) in counting mode from –60˚ to +60˚ using a dose-symmetric acquisition scheme (Hagen et al., 2017) with a total dose of 82 $e^{-}/Å^2$. The tilt series were processed with IMOD (Kremer et al., 1996). Weighted back projection was used to reconstruct the 3D tomograms after patch tracking tilt series alignment. Tomographic volumes were segmented with the convolutional neural network method implemented in EMAN2.2 (Chen et al., 2017). UCSF Chimera was used for visualizing tomographic volumes (Pettersen et al., 2021). Software used for processing tilt series and visualizing volumes was curated by SBGrid (Morin et al., 2013).

Acknowledgments: We thank Dr. Leila Foroughi and Dr. Adam Matzeger in the Department of Chemistry at the University of Michigan for the use of the Raman spectroscopy instrument and assistance. We thank the staff at the University of Michigan cryo-EM center for the use of the Morgagni instrument and assistance. We thank Dr. Haiping Sun and the Michigan Center for Materials Characterization for the use of the AFM instrument and assistance. Dr. Seung-Jae Lee at Chonbuk National University kindly provided the purified *M. caps* sMMOH.

Funding: This work was supported by grants from R01 DK111465, R01 CA250329, and R01 NS116008 to U.-S.C. A portion of this research was supported by NIH grant U24GM129547, performed at the PNCC at OHSU, and accessed through EMSL (grid.436923.9), a DOE Office of Science User Facility sponsored by the Office of Biological and Environmental Research.

Author contributions: The manuscript was written through contributions of all authors. U.-S.C. designed the research; E.A. and B.K. performed research and analyzed data; S.P. performed experiments in revision; A.E. and S.M. performed the cryo-electron tomography data collection and analysis; S.H.S. and R.H. performed the electron microscopy measurements for tilting method and SAED; E.A., B.K., and U.-S.C. wrote the manuscript. All authors have given approval to the final version of the manuscript. †E.A. and B.K. contributed equally.

Competing interests: The authors declare no competing interests.

Data and materials availability: The structural data has been deposited to the PDB and EMDB. The accession numbers of *M. caps* MMOH structures for the graphene grid and Au Quantifoil grid are PDB: 7TC8 / EMDB-25805 and PDB: 7TC7 / EMDB-25804, respectively.

The STL file for this grid transfer tool can be freely downloaded in the following link (https://drive.google.com/file/d/1Ypu8qxs3QKvii0EEzsLVLajQxGKETX9k/view?usp=sharing) and graphene grid making protocol movie (Movie S1) is also available in YouTube (https://www.youtube.com/watch?v=k2FdT7vos0M).

References

Afonine P V, Grosse-Kunstleve RW, Echols N, Headd JJ, Moriarty NW, Mustyakimov M, Terwilliger TC, Urzhumtsev A, Zwart PH, Adams PD. 2012. Towards automated crystallographic structure refinement with phenix.refine. *Acta Crystallographica Section D* **68**:352–367.

Arsiccio A, McCarty J, Pisano R, Shea J-E. 2020. Heightened Cold-Denaturation of Proteins at the Ice–Water Interface. *J Am Chem Soc* **142**:5722–5730. doi:10.1021/jacs.9b13454

Bai J, Zhong X, Jiang S, Huang Y, Duan X. 2010. Graphene nanomesh. *Nature Nanotechnology* **5**:190–194. doi:10.1038/nnano.2010.8

Bai X, McMullan G, Scheres SHW. 2015. How cryo-EM is revolutionizing structural biology. *Trends in Biochemical Sciences* **40**:49–57. doi:https://doi.org/10.1016/j.tibs.2014.10.005

Banerjee R, Jones JC, Lipscomb JD. 2019. Soluble Methane Monooxygenase. *Annual Review of Biochemistry* **88**:409–431. doi:10.1146/annurev-biochem-013118-111529

Benjamin CJ, Wright KJ, Bolton SC, Hyun S-H, Krynski K, Grover M, Yu G, Guo F, Kinzer-Ursem TL, Jiang W, Thompson DH. 2016. Selective Capture of Histidine-tagged Proteins from Cell Lysates Using TEM grids Modified with NTA-Graphene Oxide. *Scientific Reports* **6**:32500. doi:10.1038/srep32500

Bepler T, Kelley K, Noble AJ, Berger B. 2020. Topaz-Denoise: general deep denoising models for cryoEM and cryoET. *Nature Communications* **11**:5208. doi:10.1038/s41467-020-18952-1

Chen M, Dai W, Sun SY, Jonasch D, He CY, Schmid MF, Chiu W, Ludtke SJ. 2017. Convolutional neural networks for automated annotation of cellular cryo-electron tomograms. *Nature Methods 2017 14:10* **14**:983–985. doi:10.1038/nmeth.4405

Cote LJ, Kim F, Huang J. 2009. Langmuir−Blodgett Assembly of Graphite Oxide Single Layers. *J Am Chem Soc* **131**:1043–1049. doi:10.1021/ja806262m

D'Imprima E, Floris D, Joppe M, Sánchez R, Grininger M, Kühlbrandt W. 2019. Protein denaturation at the air-water interface and how to prevent it. *Elife* **8**:e42747. doi:10.7554/eLife.42747

Drulyte I, Johnson RM, Hesketh EL, Hurdiss DL, Scarff CA, Porav SA, Ranson NA, Muench SP, Thompson RF. 2018. Approaches to altering particle distributions in cryo-electron microscopy sample preparation. *Acta Crystallographica Section D* **74**:560–571.

Dubochet J. 2012. Cryo-EM—the first thirty years. *Journal of Microscopy* **245**:221–224. doi:https://doi.org/10.1111/j.1365-2818.2011.03569.x

Elango M, Thamilselvan M, Hemalatha V, Sangameswari. 2011. Structural and optical characterization on ZnS: Mn filled PMMA nanocompositesInternational Conference on Nanoscience, Engineering and Technology (ICONSET 2011). pp. 11–13. doi:10.1109/ICONSET.2011.6167899

Emsley P, Cowtan K. 2004. Coot: model-building tools for molecular graphics. *Acta Crystallographica Section D* **60**:2126–2132.

Fan X, Wang J, Zhang X, Yang Z, Zhang J-C, Zhao L, Peng H-L, Lei J, Wang H-W. 2019. Single

particle cryo-EM reconstruction of 52 kDa streptavidin at 3.2 Angstrom resolution. *Nature Communications* **10**:2386. doi:10.1038/s41467-019-10368-w

Ferrari AC, Basko DM. 2013. Raman spectroscopy as a versatile tool for studying the properties of graphene. *Nature Nanotechnology* **8**:235–246. doi:10.1038/nnano.2013.46

Gardiner AT, Naydenova K, Castro-Hartmann P, Nguyen-Phan TC, Russo CJ, Sader K, Hunter CN, Cogdell RJ, Qian P. 2021. The 2.4 Å cryo-EM structure of a heptameric light-harvesting 2 complex reveals two carotenoid energy transfer pathways. *Science Advances* **7**:eabe4650. doi:10.1126/sciadv.abe4650

Glaeser RM. 2016. Specimen Behavior in the Electron Beam In: Crowther RABT-M in E, editor. The Resolution Revolution: Recent Advances In CryoEM. Academic Press. pp. 19–50. doi:10.1016/bs.mie.2016.04.010

Grigorenko AN, Polini M, Novoselov KS. 2012. Graphene plasmonics. *Nature Photonics* **6**:749–758. doi:10.1038/nphoton.2012.262

Hagen WJH, Wan W, Briggs JAG. 2017. Implementation of a cryo-electron tomography tilt-scheme optimized for high resolution subtomogram averaging. *Journal of Structural Biology* **197**:191–198. doi:10.1016/j.jsb.2016.06.007

Han B-G, Walton RW, Song A, Hwu P, Stubbs MT, Yannone SM, Arbeláez P, Dong M, Glaeser RM. 2012. Electron microscopy of biotinylated protein complexes bound to streptavidin monolayer crystals. *Journal of Structural Biology* **180**:249–253. doi:https://doi.org/10.1016/j.jsb.2012.04.025

Han Y, Fan X, Wang H, Zhao F, Tully CG, Kong J, Yao N, Yan N. 2020. High-yield monolayer graphene grids for near-atomic resolution cryoelectron microscopy. *Proceedings of the National Academy of Sciences* **117**:1009–1014. doi:10.1073/pnas.1919114117

Huang X, Zhang L, Wen Z, Chen H, Li S, Ji G, Yin C, Sun F. 2020. Amorphous nickel titanium alloy film: A new choice for cryo electron microscopy sample preparation. *Progress in Biophysics and Molecular Biology* **156**:3–13. doi:https://doi.org/10.1016/j.pbiomolbio.2020.07.009

Kelly DF, Dukovski D, Walz T. 2010. Strategy for the Use of Affinity Grids to Prepare Non-His-Tagged Macromolecular Complexes for Single-Particle Electron Microscopy. *Journal of Molecular Biology* **400**:675–681. doi:https://doi.org/10.1016/j.jmb.2010.05.045

Kelly DF, Dukovski D, Walz T. 2008. Monolayer purification: A rapid method for isolating protein complexes for single-particle electron microscopy. *Proceedings of the National Academy of Sciences* **105**:4703–4708. doi:10.1073/pnas.0800867105

Kim H, An S, Park YR, Jang H, Yoo H, Park SH, Lee SJ, Cho U-S. 2019. MMOD-induced structural changes of hydroxylase in soluble methane monooxygenase. *Science Advances* **5**:eaax0059. doi:10.1126/sciadv.aax0059

Kopp DA, Gassner GT, Blazyk JL, Lippard SJ. 2001. Electron-Transfer Reactions of the Reductase Component of Soluble Methane Monooxygenase from Methylococcus capsulatus (Bath). *Biochemistry* **40**:14932–14941. doi:10.1021/bi015556t

Kremer JR, Mastronarde DN, McIntosh JR. 1996. Computer visualization of three-dimensional image data using IMOD. *J Struct Biol* **116**:71–76. doi:10.1006/JSBI.1996.0013

Kühlbrandt W. 2014. Cryo-EM enters a new era. *Elife* **3**:e03678. doi:10.7554/eLife.03678

Kumar A, Sengupta N, Dutta S. 2021. Simplified Approach for Preparing Graphene Oxide TEM Grids for Stained and Vitrified Biomolecules. *Nanomaterials* **11**:643. doi:10.3390/nano11030643

Lawson CL, Berman HM, Chiu W. 2020. Evolving data standards for cryo-EM structures. *Structural Dynamics* **7**:14701. doi:10.1063/1.5138589

Lee C, Wei X, Kysar JW, Hone J. 2008. Measurement of the elastic properties and intrinsic strength of monolayer graphene. *Science* **321**:385–8. doi:10.1126/science.1157996

Lee G-H, Cooper RC, An SJ, Lee S, van der Zande A, Petrone N, Hammerberg AG, Lee C, Crawford B, Oliver W, Kysar JW, Hone J. 2013. High-strength chemical-vapor-deposited graphene and grain boundaries. *Science* **340**:1073–6. doi:10.1126/science.1235126

Lee SJ, McCormick MS, Lippard SJ, Cho U-S. 2013. Control of substrate access to the active site in methane monooxygenase. *Nature* **494**:380–384. doi:10.1038/nature11880

Lin L, Zhang J, Su H, Li J, Sun L, Wang Z, Xu F, Liu C, Lopatin S, Zhu Y, Jia K, Chen S, Rui D, Sun J, Xue R, Gao P, Kang N, Han Y, Xu HQ, Cao Y, Novoselov KS, Tian Z, Ren B, Peng H, Liu Z. 2019. Towards super-clean graphene. *Nature Communications* **10**:1912. doi:10.1038/s41467-019-09565-4

Lin Z, Ye X, Han J, Chen Q, Fan P, Zhang H, Xie D, Zhu H, Zhong M. 2015. Precise Control of the Number of Layers of Graphene by Picosecond Laser Thinning. *Scientific Reports* **5**:11662. doi:10.1038/srep11662

Liu N, Zhang J, Chen Y, Liu C, Zhang X, Xu K, Wen J, Luo Z, Chen S, Gao P, Jia K, Liu Z, Peng H, Wang HW. 2019. Bioactive Functionalized Monolayer Graphene for High-Resolution Cryo-Electron Microscopy. *J Am Chem Soc* **141**:4016–4025. doi:10.1021/jacs.8b13038

Llaguno MC, Xu H, Shi L, Huang N, Zhang H, Liu Q, Jiang Q-X. 2014. Chemically functionalized carbon films for single molecule imaging. *Journal of Structural Biology* **185**:405–417. doi:https://doi.org/10.1016/j.jsb.2014.01.006

Ma H, Hsiao BS, Chu B. 2016. Modified Cellulose BT - Encyclopedia of Membranes In: Drioli E, Giorno L, editors. Berlin, Heidelberg: Springer Berlin Heidelberg. pp. 1320–1321. doi:10.1007/978-3-662-44324-8_390

Malard LM, Pimenta MA, Dresselhaus G, Dresselhaus MS. 2009. Raman spectroscopy in graphene. *Physics Reports* **473**:51–87. doi:https://doi.org/10.1016/j.physrep.2009.02.003

Mastronarde DN. 2005. Automated electron microscope tomography using robust prediction of specimen movements. doi:10.1016/j.jsb.2005.07.007

Merkx M, Kopp DA, Sazinsky MH, Blazyk JL, Müller J, Lippard SJ. 2001. Dioxygen Activation and Methane Hydroxylation by Soluble Methane Monooxygenase: A Tale of Two Irons and Three Proteins. *Angewandte Chemie International Edition* **40**:2782–2807. doi:https://doi.org/10.1002/1521-3773(20010803)40:15<2782::AID-ANIE2782>3.0.CO;2-P

Merkx M, Lippard SJ. 2002. Why OrfY? *Journal of Biological Chemistry* **277**:5858–5865. doi:10.1074/jbc.M107712200

Morin A, Eisenbraun B, Key J, Sanschagrin PC, Timony MA, Ottaviano M, Sliz P. 2013.

Collaboration gets the most out of software. *Elife* **2**. doi:10.7554/ELIFE.01456

Naydenova K, Jia P, Russo CJ. 2020. Cryo-EM with sub–1 Å specimen movement. *Science (1979)* **370**:223–226. doi:10.1126/science.abb7927

Naydenova K, Peet MJ, Russo CJ. 2019. Multifunctional graphene supports for electron cryomicroscopy. *Proc Natl Acad Sci U S A* **116**:11718–11724. doi:10.1073/pnas.1904766116

Novoselov KS, Geim AK, Morozov S V, Jiang D, Zhang Y, Dubonos S V, Grigorieva I V, Firsov AA. 2004. Electric Field Effect in Atomically Thin Carbon Films. *Science (1979)* **306**:666–669.

Palovcak E, Wang F, Zheng SQ, Yu Z, Li S, Betegon M, Bulkley D, Agard DA, Cheng Y. 2018. A simple and robust procedure for preparing graphene-oxide cryo-EM grids. *Journal of Structural Biology* **204**:80–84. doi:10.1016/j.jsb.2018.07.007

Park H, Brown PR, Bulović V, Kong J. 2012. Graphene As Transparent Conducting Electrodes in Organic Photovoltaics: Studies in Graphene Morphology, Hole Transporting Layers, and Counter Electrodes. *Nano Letters* **12**:133–140. doi:10.1021/nl2029859

Pathak M, Kweon H, Deo M, Huang H. 2017. Kerogen Swelling and Confinement: Its implication on Fluid Thermodynamic Properties in Shales. *Scientific Reports* **7**:12530. doi:10.1038/s41598-017-12982-4

Paulsen KE, Liu Y, Fox BG, Lipscomb JD, Munck E, Stankovich MT. 1994. Oxidation-reduction potentials of the methane monooxygenase hydroxylase component from Methylosinus trichosporium OB3b. *Biochemistry* **33**:713–722. doi:10.1021/bi00169a013

Pettersen EF, Goddard TD, Huang CC, Couch GS, Greenblatt DM, Meng EC, Ferrin TE. 2004. UCSF Chimera—A visualization system for exploratory research and analysis. *Journal of Computational Chemistry* **25**:1605–1612. doi:https://doi.org/10.1002/jcc.20084

Pettersen EF, Goddard TD, Huang CC, Meng EC, Couch GS, Croll TI, Morris JH, Ferrin TE. 2021. UCSF ChimeraX: Structure visualization for researchers, educators, and developers. *Protein Science* **30**:70–82. doi:10.1002/PRO.3943

Pirkle A, Chan J, Venugopal A, Hinojos D, Magnuson CW, McDonnell S, Colombo L, Vogel EM, Ruoff RS, Wallace RM. 2011. The effect of chemical residues on the physical and electrical properties of chemical vapor deposited graphene transferred to SiO 2. *Applied Physics Letters* **99**:122108. doi:10.1063/1.3643444

Punjani A, Rubinstein JL, Fleet DJ, Brubaker MA. 2017. cryoSPARC: algorithms for rapid unsupervised cryo-EM structure determination. *Nature Methods* **14**:290–296. doi:10.1038/nmeth.4169

Rhinow D, Büenfeld M, Weber N-E, Beyer A, Gölzhäuser A, Kühlbrandt W, Hampp N, Turchanin A. 2011. Energy-filtered transmission electron microscopy of biological samples on highly transparent carbon nanomembranes. *Ultramicroscopy* **111**:342–349. doi:https://doi.org/10.1016/j.ultramic.2011.01.028

Rhinow D, Kühlbrandt W. 2008. Electron cryo-microscopy of biological specimens on conductive titanium–silicon metal glass films. *Ultramicroscopy* **108**:698–705. doi:https://doi.org/10.1016/j.ultramic.2007.11.005

Rice WJ, Cheng A, Noble AJ, Eng ET, Kim LY, Carragher B, Potter CS. 2018. Routine determination of ice thickness for cryo-EM grids. *Journal of Structural Biology* **204**:38–44. doi:https://doi.org/10.1016/j.jsb.2018.06.007

Rosenzweig AC, Brandstetter H, Whittington DA, Nordlund P, Lippard SJ, Frederick CA. 1997. Crystal structures of the methane monooxygenase hydroxylase from Methylococcus capsulatus (Bath): Implications for substrate gating and component interactions. *Proteins: Structure, Function, and Bioinformatics* **29**:141–152. doi:https://doi.org/10.1002/(SICI)1097-0134(199710)29:2<141::AID-PROT2>3.0.CO;2-G

Rosenzweig AC, Frederick CA, Lippard SJ, Nordlund P auml;r. 1993. Crystal structure of a bacterial non-haem iron hydroxylase that catalyses the biological oxidation of methane. *Nature* **366**:537–543. doi:10.1038/366537a0

Russo CJ, Passmore LA. 2016. Progress towards an optimal specimen support for electron cryomicroscopy. *Current Opinion in Structural Biology* **37**:81–89. doi:https://doi.org/10.1016/j.sbi.2015.12.007

Russo CJ, Passmore LA. 2014. Controlling protein adsorption on graphene for cryo-EM using low-energy hydrogen plasmas. *Nature Methods* **11**:649–652. doi:10.1038/nmeth.2931

Sazinsky MH, Lippard SJ. 2006. Correlating Structure with Function in Bacterial Multicomponent Monooxygenases and Related Diiron Proteins. *Accounts of Chemical Research* **39**:558–566. doi:10.1021/ar030204v

Sazinsky MH, Lippard SJ. 2005. Product Bound Structures of the Soluble Methane Monooxygenase Hydroxylase from Methylococcus capsulatus (Bath): Protein Motion in the α-Subunit. *J Am Chem Soc* **127**:5814–5825. doi:10.1021/ja044099b

Scheres SHW. 2012. RELION: Implementation of a Bayesian approach to cryo-EM structure determination. *Journal of Structural Biology* **180**:519–530. doi:https://doi.org/10.1016/j.jsb.2012.09.006

Sirajuddin S, Rosenzweig AC. 2015. Enzymatic Oxidation of Methane. *Biochemistry* **54**:2283–2294. doi:10.1021/acs.biochem.5b00198

Suk JW, Kitt A, Magnuson CW, Hao Y, Ahmed S, An J, Swan AK, Goldberg BB, Ruoff RS. 2011. Transfer of CVD-Grown Monolayer Graphene onto Arbitrary Substrates. *ACS Nano* **5**:6916–6924. doi:10.1021/nn201207c

Sun F. 2018. Orienting the future of bio-macromolecular electron microscopy. *Chinese Physics B* **27**:063601. doi:10.1088/1674-1056/27/6/063601

Tan PH, Han WP, Zhao WJ, Wu ZH, Chang K, Wang H, Wang YF, Bonini N, Marzari N, Pugno N, Savini G, Lombardo A, Ferrari AC. 2012. The shear mode of multilayer graphene. *Nature Materials* **11**:294–300. doi:10.1038/nmat3245

Tan YZ, Baldwin PR, Davis JH, Williamson JR, Potter CS, Carragher B, Lyumkis D. 2017. Addressing preferred specimen orientation in single-particle cryo-EM through tilting. *Nature Methods* **14**:793–796. doi:10.1038/nmeth.4347

Wang F, Liu Y, Yu Z, Li S, Feng S, Cheng Y, Agard DA. 2020. General and robust covalently linked graphene oxide affinity grids for high-resolution cryo-EM. *Proceedings of the National*

Academy of Sciences **117**:24269–24273. doi:10.1073/pnas.2009707117

Whittington DA, Lippard SJ. 2001. Crystal Structures of the Soluble Methane Monooxygenase Hydroxylase from Methylococcus capsulatus (Bath) Demonstrating Geometrical Variability at the Dinuclear Iron Active Site. *J Am Chem Soc* **123**:827–838. doi:10.1021/ja003240n

Whittington DA, Rosenzweig AC, Frederick CA, Lippard SJ. 2001. Xenon and Halogenated Alkanes Track Putative Substrate Binding Cavities in the Soluble Methane Monooxygenase Hydroxylase,. *Biochemistry* **40**:3476–3482. doi:10.1021/bi0022487

Wu J-B, Zhang X, Ijäs M, Han W-P, Qiao X-F, Li X-L, Jiang D-S, Ferrari AC, Tan P-H. 2014. Resonant Raman spectroscopy of twisted multilayer graphene. *Nature Communications* **5**:5309. doi:10.1038/ncomms6309

Yao X, Fan X, Yan N. 2020. Cryo-EM analysis of a membrane protein embedded in the liposome. *Proceedings of the National Academy of Sciences* **117**:18497–18503. doi:10.1073/pnas.2009385117

Yu G, Li K, Huang P, Jiang X, Jiang W. 2016. Antibody-Based Affinity Cryoelectron Microscopy at 2.6-Å Resolution. *Structure* **24**:1984–1990. doi:10.1016/j.str.2016.09.008

Zhang J, Lin L, Sun L, Huang Y, Koh AL, Dang W, Yin J, Wang M, Tan C, Li T, Tan Z, Liu Z, Peng H. 2017. Clean Transfer of Large Graphene Single Crystals for High-Intactness Suspended Membranes and Liquid Cells. *Advanced Materials* **29**:1700639. doi:https://doi.org/10.1002/adma.201700639

Zhang J, Sun L, Jia K, Liu X, Cheng T, Peng H, Lin L, Liu Z. 2020. New Growth Frontier: Superclean Graphene. *ACS Nano* **14**:10796–10803. doi:10.1021/acsnano.0c06141

Zhang K. 2016. Gctf: Real-time CTF determination and correction. *Journal of Structural Biology* **193**:1–12. doi:https://doi.org/10.1016/j.jsb.2015.11.003

Zhang Y, Ren W, Jiang Z, Yang S, Jing W, Shi P, Wu X, Ye Z-G. 2014. Low-temperature remote plasma-enhanced atomic layer deposition of graphene and characterization of its atomic-level structure. *Journal of Materials Chemistry C* **2**:7570–7574. doi:10.1039/C4TC00849A

Zivanov J, Nakane T, Forsberg BO, Kimanius D, Hagen WJH, Lindahl E, Scheres SHW. 2018. New tools for automated high-resolution cryo-EM structure determination in RELION-3. *Elife* **7**:e42166. doi:10.7554/eLife.42166

Figures and Tables

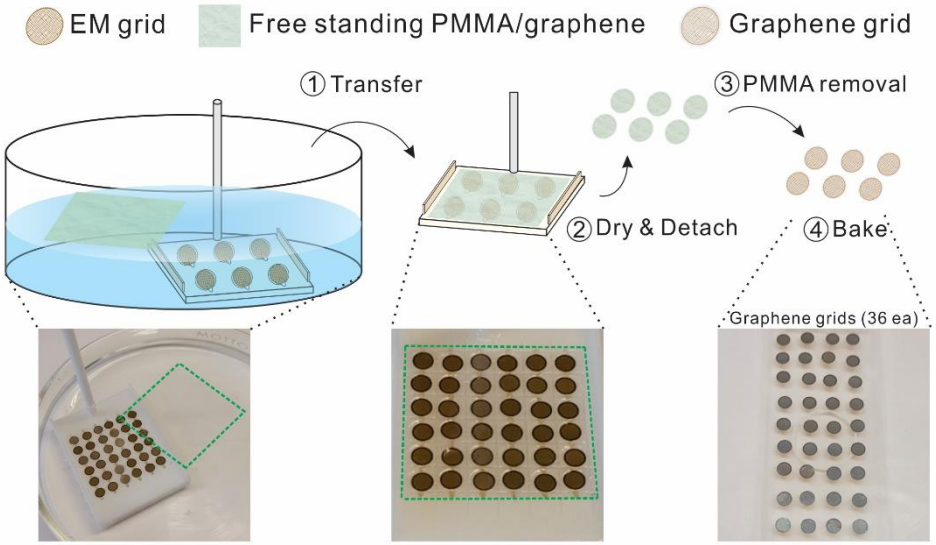

Figure 1. Schematic and photographic views of graphene grid production. Green dash square in photographs denotes the PMMA/graphene region.

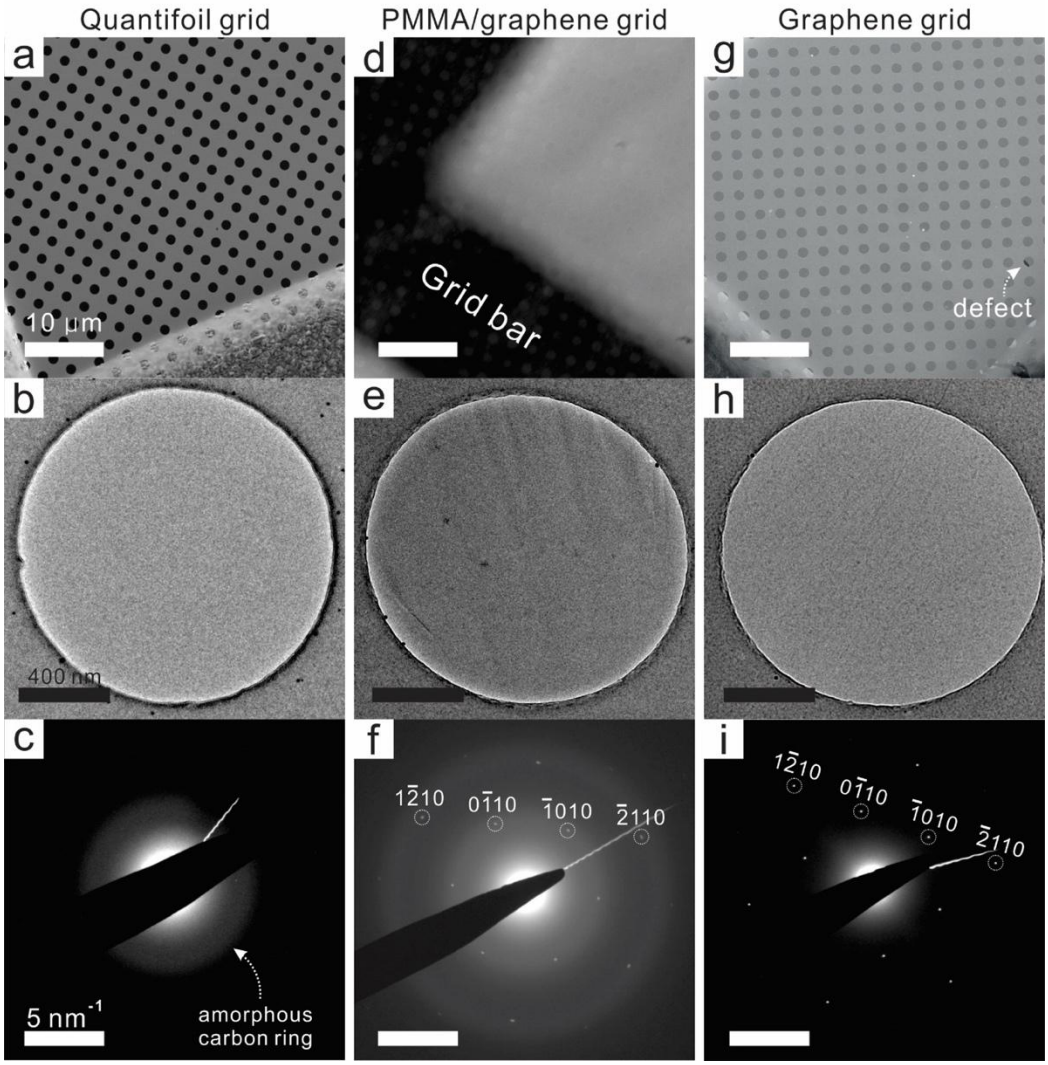

Figure 2. (a-c) Left-side images are from untreated commercial Au Quantifoil grids. (d-f) Mid-side images are from PMMA/graphene-coated Au Quantifoil grids. (g-i) Right-side images are PMMA-free graphene grids after rinsing/baking steps. (a, d, g) Scale bars in SEM image represent 10 μm. (b, e, h) Scale bars in TEM image represent 400 nm. (c, f, i) Scale bars in SAED images represent 5 nm^{-1}.

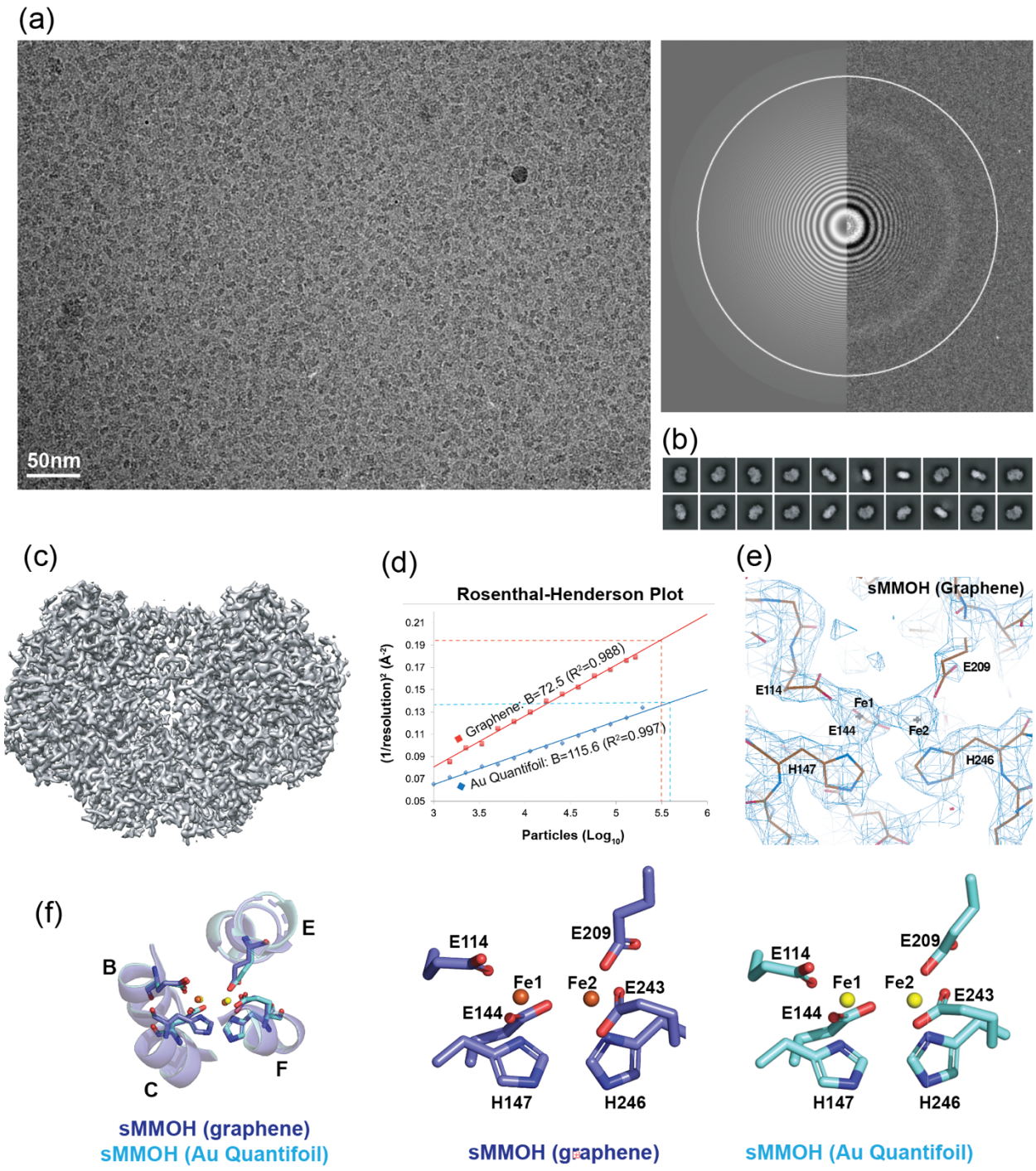

Figure 3. (a) Representative microscopic image of *M. caps* sMMOH in the graphene grid (300 kV) with the image of the power spectrum. (b) Top 20 2D classes selected from 200 classes of sMMOH in the graphene grid. (c) Reconstructed 3D cryo-EM map (2.4 Å resolution) of sMMOH in the graphene grid. (d) The Rosenthal-Henderson plot of sMMOH structures determined using the Au Quantifoil (blue diamond-shape) and graphene (red square) grids. Dashed lines indicate the

particles used for the final refinement. (e) Cryo-EM map of non-heme di-iron center of sMMOH (graphene grid) coordinated by four Glutamates and two histidines. The image was captured by COOT (f) Structural overlay of sMMOH four-helix bundle (helix B, C, E, and F) and (g) Coordinating residues (four glutamates and two histidines) determined by Au Quantifoil (cyan; yellow for two irons) and graphene (blue; orange for two irons) grids.

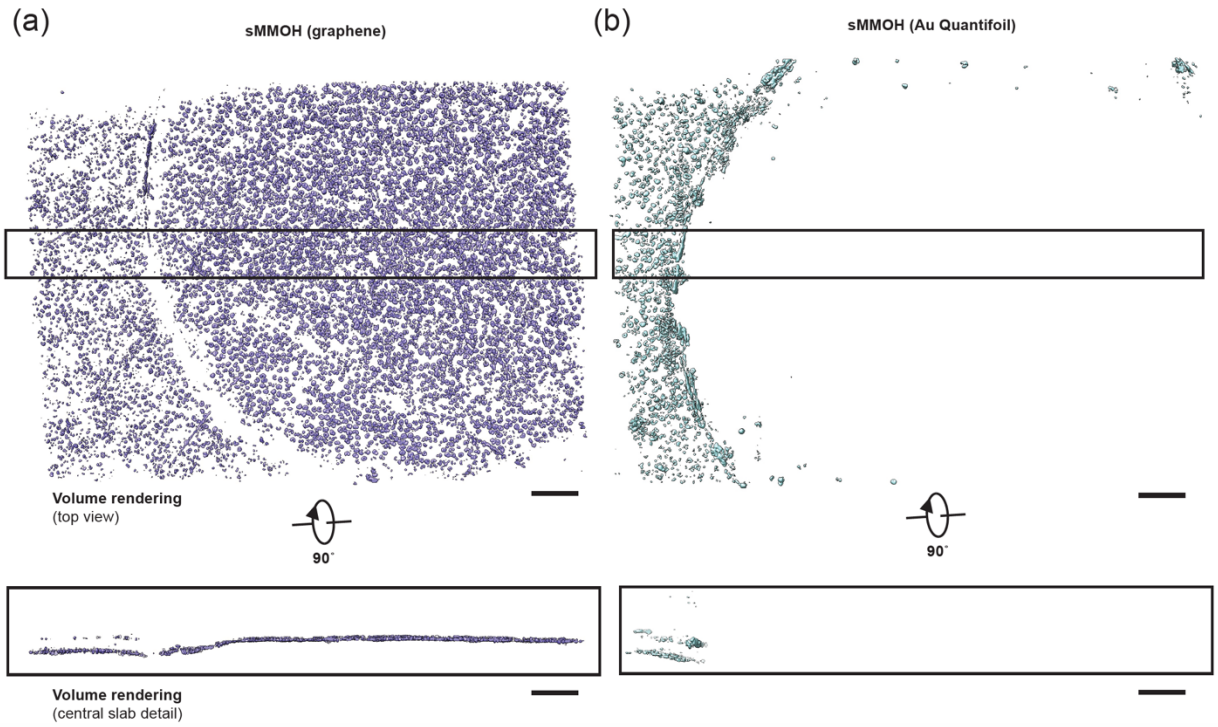

Figure 4. *M. caps* sMMOH particle distribution on plunge-frozen graphene-coated and Au Quantifoil grids. (a) Top and central slab views of segmented sMMOH particles (purple) from a graphene-coated grid hole tomogram. (b) Top and central slab views of segmented sMMOH particles (cyan) from an Au Quantifoil grid hole tomogram. Scale bar, 100nm.

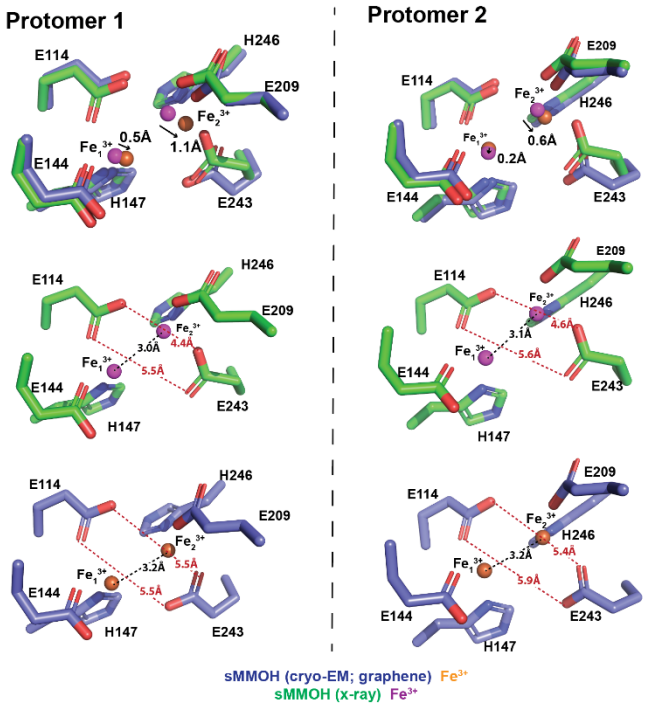

Figure 5. Non-heme di-iron center geometry comparison in between x-ray structure (PDB ID: 1MTY) and cryo-EM structure (graphene grid). The di-iron center geometry of both sMMOH protomers (protomer 1 and 2) was compared.